J Adv Ceram

Research Article

A high-entropy strategy for enhancing energy storage performance and enabling ultrafast discharge in tungsten bronze ceramics

Wenzhi Ning[1], Jianming Xie[1], Liupan Tang[1], Chongdong Dong[1], Yingzhi Meng[1], Changzheng Hu[1,2,3]✉, Liang Fang[1,2,3], Laijun Liu[1,2,3]

Cite this article: Ning W, Xie J, Tang L, et al. *J Adv Ceram* 2026, **15**(4): 9221260. https://doi.org/10.26599/JAC.2026.9221260

ABSTRACT: Dielectric ceramics, as core materials for energy storage capacitors, have been widely utilized across various fields owing to their high-power density and ultrafast charge–discharge characteristics. In this study, a synergistic strategy combining high-entropy and bandgap engineering was employed to successfully prepare lead-free high-entropy dielectric ceramics with a tungsten bronze structure having the chemical composition $Ba_{2.38}Sr_{2.12}Sm_{0.5}Gd_{0.5}Ti_1Zr_1Nb_{8-x}Ta_xO_{30}$ (Ta_x, x = 0, 0.5, 1, and 1.5). The long-range ferroelectric order is effectively disrupted through high-entropy design, which enhances cationic disorder and thereby promotes relaxor ferroelectric behavior. Meanwhile, the synergistic effects of grain refinement, increased activation energy for electrical conductivity, and an enlarged bandgap significantly enhance the material's breakdown strength. Through the collective effects of these mechanisms, the energy storage performance of the ceramics is significantly enhanced, with a recoverable energy density of 7.93 J·cm^{-3} and an energy efficiency of 94.25% achieved at x = 0.5. Furthermore, the material demonstrates a current density of approximately 971.34 A·cm^{-2}, a power density of 155.41 MW·cm^{-3}, an ultrafast discharge time of 1.56 μs, and a discharge energy density of 5.20 J·cm^{-3}. This study presents an effective approach for developing high-performance dielectric ceramic materials, highlighting their promising potential for application in advanced pulsed power systems.

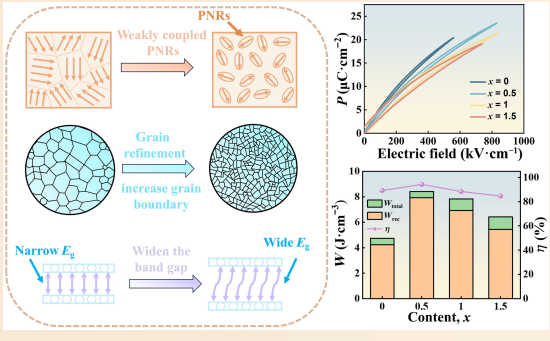

KEYWORDS: high-entropy; energy storage; high efficiency; tungsten bronze structure

1 Introduction

As environmental pollution becomes increasingly severe and energy shortages intensify, energy storage technology has emerged as a major research focus for a broad community of scholars. Dielectric ceramics, distinguished by their ultrafast discharge rates, high power density, and exceptional high-temperature stability, occupy a prominent position in the field of energy storage material research [1–6]. Nevertheless, their practical application remains constrained by critical challenges, including low recoverable energy density and inadequate energy efficiency [7–11].

The chemical formula of the tetragonal tungsten bronze (TTB) structure is $(A1)_2(A2)_4(C)_4(B1)_2(B2)_8O_{30}$. Compared to the perovskite structure, although TTB exhibits lower polarization strength and a lower breakdown field due to abnormal grain growth, it possesses a more open crystal framework composed of interconnected oxygen octahedra. Owing to the presence of multiple cation sites, such as A1, A2, C, B1, and B2, TTB-structured ceramics demonstrate significant tunability in their properties. This structural complexity enables researchers to finely adjust polarization behavior at the atomic scale through strategies such as "high-entropy design" and "site doping". In recent studies on TTB materials, their energy storage performance has become comparable to that of mainstream perovskite materials [12–16]. $Sr_xBa_{1-x}Nb_2O_6$ (SBN) is a prototypical unfilled TTB material featuring approximately 1/6 vacancies at the A-sites. In this structure, the larger Ba^{2+} ions preferentially occupy the pentagonal A2 sites, while the smaller Sr^{2+} ions are distributed across both the A1 and A2 sites. The relaxor behavior observed in TTB systems, including SBN, is primarily attributed to lattice distortions caused by this random cation distribution. Specifically, for

[1] Key Laboratory of New Processing Technology for Nonferrous Metal & Materials, Ministry of Education, College of Materials Science and Engineering, Guilin University of Technology, Guilin 541004, China. [2] Guangxi Key Laboratory of Optical and Electronic Materials and Devices, Guilin University of Technology, Guilin 541004, China. [3] Collaborative Innovation Center for Exploration of Nonferrous Metal Deposits and Efficient Utilization of Resources in Guangxi, Guilin University of Technology, Guilin 541004, China.

✉ Corresponding author. E-mail: huchzh@foxmail.com

Received: November 21, 2025; Revised: February 2, 2026; Accepted: February 8, 2026

SBN—particularly for the $Sr_{0.67}Ba_{0.33}Nb_2O_6$ composition—the relaxor character stems from the size mismatch between Sr^{2+} and Ba^{2+} at the A2 sites. This ionic size disparity displaces neighboring oxygen atoms, generating a net polarization. particularly for the $Sr_{0.67}Ba_{0.33}Nb_2O_6$ composition—the relaxor character stems from the size mismatch between Sr^{2+} and Ba^{2+} at the A2 sites. On a microscopic mechanism level, random fluctuations in the internal electric field lead to broad octahedral tilting along the *c*-axis, which alleviates the lattice strain caused by the size mismatch of A-site ions and significantly affects the ferroelectric properties of the material. Based on this understanding, modulating relaxor behavior through A-site doping has become an important approach. For example, introducing rare-earth ions with higher electronegativity (such as Gd^{3+}) can preferentially tune the relaxor dynamics in the SBN matrix, effectively enhancing ferroelectric polarization. Further doping with Sm^{3+}, which has a smaller ionic radius (1.24 Å, significantly smaller than Ba^{2+} at 1.61 Å and Sr^{2+} at 1.44 Å), introduces stronger lattice distortion and exacerbates chemical disorder and charge imbalance at the A-sites, thereby influencing its ferroelectric and relaxor properties at a deeper level [17,18].

The high-entropy design strategy involves the simultaneous introduction of multiple heterovalent ions into tungsten bronze ceramics, which triggers strong structural disorder and atomic mismatch, thereby forming "disordered polarization functional units" characterized by local composition fluctuations and cation displacements. This structural change disrupts the long-range ferroelectric order, transforming it into finely sized and dynamically active polar nanoregions (PNRs). These nanoregions not only significantly reduce the energy barrier for domain switching but also weaken interdomain coupling, thereby delaying polarization saturation, suppressing the formation of large domains, and facilitating rapid polarization recovery after the electric field is removed. Simultaneously, lattice distortion and grain refinement induced by the high-entropy effect further enhance the material's insulating properties and densification, markedly improving the breakdown electric field. Benefiting from these synergistic mechanisms, the energy storage performance of the ceramic sample is notably enhanced [19,20]. For example, Duan *et al.* [21] reported high-entropy ceramics with the composition $Sr_{0.35}Ba_{0.35}Na_{0.1}Ca_{0.1}Bi_{0.1}Nb_{1.8}Ta_{0.2}O_6$, achieving a recoverable energy density (W_{rec}) of 10.6 J·cm^{-3} and an efficiency (η) of 96.2% at an electric field of 760 kV·cm^{-1}. The random distribution of cations on the A- and B-sites facilitates complex local interactions, fragmenting the long-range ferroelectric order into diverse PNRs characterized by compositional fluctuations and cation displacements. These PNRs lower the energy barrier for domain switching, weaken interdomain coupling, and consequently delay polarization saturation, reduce energy loss, and enhance the breakdown electric field (E_b). In another study, employing a combined strategy of high-entropy design and bandgap engineering, Gao *et al.* [22] successfully fabricated $Ba_{0.4}Sr_{0.3}Ca_{0.3}Nb_{1.7}Ta_{0.3}O_6$ high-entropy ceramics, which achieved a W_{rec} of 8.9 J·cm^{-3} and an η of 93%, along with excellent thermal stability over a 105 °C range and outstanding cycling stability. The molar configurational entropy (ΔS_{config}) is given by Eq. (1) [23]:

$$\Delta S_{config} = -R\left(\left(\sum_{a=1}^{n} x_a \ln x_a\right)_{A\text{-site}} + \left(\sum_{b=1}^{n} x_b \ln x_b\right)_{B\text{-site}} + 3\left(\sum_{c=1}^{n} x_c \ln x_c\right)_{O\text{-site}}\right) \quad (1)$$

where R stands for the universal gas constant, a, b, and c represent the different chemical species on the A-site, B-site, and O-site, respectively, and x_a, x_b, and x_c are the molar fractions of ions residing at the A, B, and O sites. The entropy classification is defined as follows: A material is considered low-entropy if $\Delta S_{config} < 0.69R$, medium-entropy if $0.69R \le \Delta S_{config} < 1.61R$, and high-entropy if $\Delta S_{config} \ge 1.61R$.

The essence of bandgap engineering lies in precisely modulating a material's band structure through doping strategies, thereby optimizing its electrical and dielectric properties. Specifically, widening the bandgap—i.e., increasing the energy barrier that electrons must overcome to transition from the valence band to the conduction band—significantly reduces the intrinsic carrier concentration and electrical conductivity. This reduction enhances the dielectric breakdown strength and consequently raises the intrinsic breakdown electric field. The application of bandgap engineering serves to enhance not only the energy storage density and efficiency of the material but also its stability under extreme temperatures. This approach provides a critical material foundation for the development of high-performance, highly reliable electronic and energy-related devices [22].

In this study, the energy storage performance of TTB-structured $Ba_{2.38}Sr_{2.12}Sm_{0.5}Gd_{0.5}Ti_1Zr_1Nb_{8-x}Ta_xO_{30}$ (Ta_x, x = 0, 0.5, 1, and 1.5) ceramics was enhanced by integrating a high-entropy strategy with bandgap engineering (Fig. 1). The incorporation of Ta_2O_5, which possesses a high bandgap, effectively increased the overall bandgap width of the material, thereby improving its breakdown electric field strength. Simultaneously, the configurational entropy rose from 2.04*R* to 2.35*R*, inducing a distinct "cocktail effect" that further optimized the energy storage characteristics of the $Ba_{0.4}Sr_{0.6}Nb_2O_6$-based ceramics. As a result, this material system achieved outstanding overall energy storage performance, delivering a recoverable energy density of 7.93 J·cm^{-3} and a high energy efficiency of up to 94.25%.

2 Experimental

The $Ba_{2.38}Sr_{2.12}Sm_{0.5}Gd_{0.5}Ti_1Zr_1Nb_{8-x}Ta_xO_{30}$ ceramics were prepared using the following composition: $BaCO_3$ (99.95%), $SrCO_3$ (99.95%), Sm_2O_3 (99.99%), Gd_2O_3 (99.99%), ZrO_2 (99.99%), TiO_2 (99.99%), Ta_2O_5 (99.99%), and Nb_2O_5 (99.99%). The starting reagents were precisely weighed according to the stoichiometric ratio. The powder mixture was then ball-milled for 12 h in anhydrous ethanol with ZrO_2 milling media using a high-energy ball mill. The resulting slurry was subsequently dried at 120 °C and finally calcined at 1000 °C for 2 h. The calcined product underwent a second round of ball milling for another 12 h and was dried again. The resulting dried powder was compacted into pellets with a diameter of 8 mm by cold isostatic pressing, followed by sintering in the temperature range of 1350–1400 °C for 6 h to obtain the final ceramic samples. The phase composition of the ceramics was examined by an X-ray diffractometer (Cu Kα1 radiation; PANalytical Empyrean, Empyrean, the Netherlands) over a 2θ range of 10°–120°, followed by Rietveld refinement using Fullprof software. Raman spectroscopy was performed on a confocal laser Raman microscope (DXR, Thermo Fisher Scientific, USA) with a 532 nm laser source. The surface morphology of the ceramics was observed using a scanning electron microscope (Hitachi S-4800, Hitachi, Japan), and the grain size was determined via Nano Measurer software. To evaluate the electrical properties, the ceramic samples were polished, coated with silver paste electrodes on both sides, and fired at 650 °C for 30 min. The sample dimensions for the electrical characterizations in this work were as

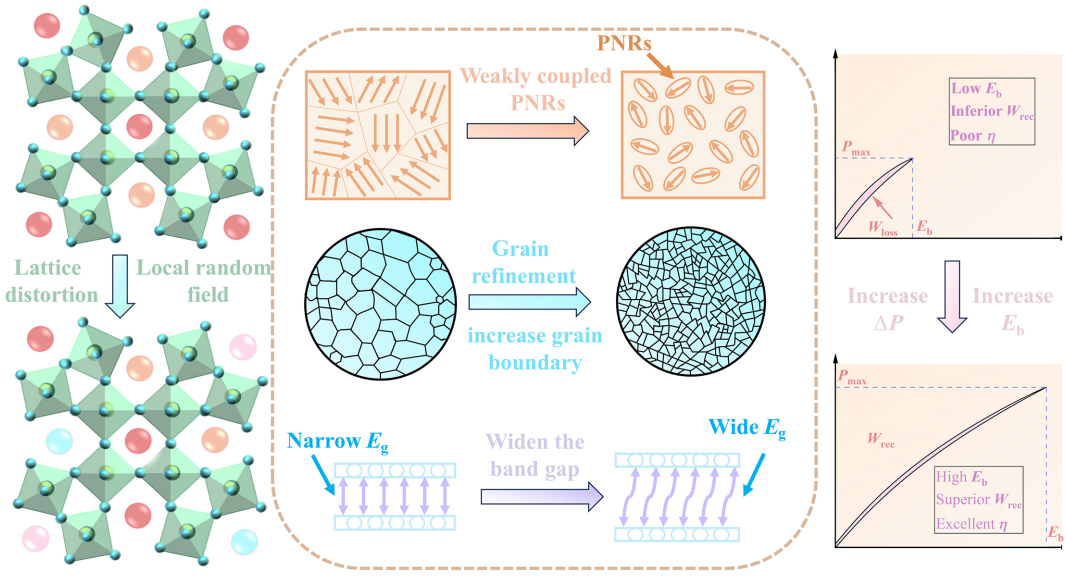

Fig. 1 Schematic of synergistic tuning in energy storage via bandgap and high-entropy effects.

follows: For dielectric measurements, the samples were approximately 1.0 mm in thickness with electrodes 3 mm in diameter; for ferroelectric tests, the samples had a thickness of 0.06±0.02 mm and electrode diameters of 2 mm. The complex impedance of the ceramic samples was characterized from 20 to 10^6 Hz at 600–680 °C using a precision LCR (inductance L, capacitance C, resistance R) meter (E4980AL, Agilent, USA), and the data were analyzed with Z-View software. Ultraviolet–Visible (UV–Vis) diffuse reflectance spectra were collected on a spectrophotometer (Model 3600, Shimadzu, Japan). The dielectric constant (ε_r) and loss tangent (tanδ) were measured over a temperature range of −150 to 200 °C and a frequency range of 1 kHz to 1 MHz via a precision LCR meter (TZDM-200-300, Harbin Julang Technology, China). Unipolar *P*–*E* ferroelectric loops were measured at 10 Hz using a ferroelectric tester (TF2000E analyzer, air ACCT Systems GmbH, Germany), both at room temperature and from 30 to 180 °C. The charge–discharge performance was tested under overdamped conditions (load resistance: 10 kΩ) using a charge–discharge test system (PK-CPR1701, PolyK Technologies, USA), while underdamped testing (load resistance: 3 Ω) was conducted with a dielectric charge–discharge test system (CFD-005, GoGo Instrument Technology, China). Selected-area electron diffraction (SAED) patterns and high-resolution transmission electron microscopy (HRTEM) images were acquired using a transmission electron microscope (TEM; 2100F, Japan Electron Optics Laboratory, Japan). The dynamic response of the ceramic samples to an applied electric field was observed by a piezoresponse force microscope (PFM; MFP-3D, Oxford Instruments Technology, USA).

3 Results and discussion

Figure 2(a) presents the X-ray diffraction (XRD) patterns of the Ta_x ceramics, confirming phase-pure TTB structures (space group *P4bm*). These results indicate the successful incorporation of Sm^{3+}, Gd^{3+}, Zr^{4+}, Ti^{4+}, and Ta^{5+} cations into the TTB host lattice, forming homogeneous solid solutions across the composition series. As depicted in Fig. 2(b), the Bragg reflection at approximately 32° in 2θ progressively moved toward larger angles with increasing *x*, suggesting lattice contraction. For a deeper understanding of structural changes, Rietveld analysis was conducted, with outcomes illustrated in Figs. S1(a)–S1(d) in the Electronic Supplementary Material (ESM) and Table 1. R_p is the profile factor, and R_{wp} is the weighted profile factor. Their values serve as key criteria for judging the correctness of the model in ceramic structure analysis. R_p and R_{wp} are both under 10%, confirming the credibility of the proposed models. This phenomenon suggests amplified deformation of [BO_6] octahedra, which favors the enhancement of relaxor characteristics. While Ta^{5+} and Nb^{5+} possess identical ionic sizes (0.64 Å for sixfold coordination), Ta^{5+} possesses higher electronegativity, leading to a shorter Ta–O bond length compared to Nb–O. This enhanced covalency consequently reduces the unit cell dimensions [24].

Raman spectroscopy was conducted to probe the structural and phase changes in the ceramic samples with varying compositions. The acquired spectra were deconvoluted using Gaussian functions. The corresponding outcomes are displayed in Fig. 2(c). In line with established reports [25], the Raman spectral range from 20 to 1000 cm^{-1} is typically deconvoluted into three distinct zones. The low-frequency zone (< 200 cm^{-1}) is dominated by lattice vibrations stemming from the displacement of A-site cations relative to BO_6 units. The intermediate zone (200–400 cm^{-1}) is primarily governed by O–B–O bending modes (ν_5), while the zone of > 400 cm^{-1} is assigned to B–O stretching modes (ν_2 and ν_1). The observed Raman spectra for all compositions show broad and diffuse bands, which signify increased compositional randomness and a depressed unit cell polarization resulting from the stochastic distribution of cations among the A-site and B-site positions. Figures 2(d) and 2(e) depict the evolution of the Raman shift positions and FWHM for the ν_2 and ν_5 modes as a function of tantalum concentration. A continuous decrease in Raman shift is observed for both modes with greater Ta incorporation, implying a reduction in unit cell polarization [26]. Moreover, elevated Ta content results in a progressive expansion of the spectral linewidth (full width at half maximum (FWHM)), which is consistent with considerable lattice deformation and strengthened coupling among neighboring BO_6 polyhedra. The enhanced interpolyhedral coupling, concomitant with the increased structural distortion, demonstrates that the introduction of Ta^{5+} cations raises the configurational entropy and amplifies the structural disorder. This effect, in turn, disrupts the long-range ferroelectric domain ordering and aggravates the distortion of the B-site octahedra, thereby promoting the emergence of relaxor ferroelectric behavior [14].

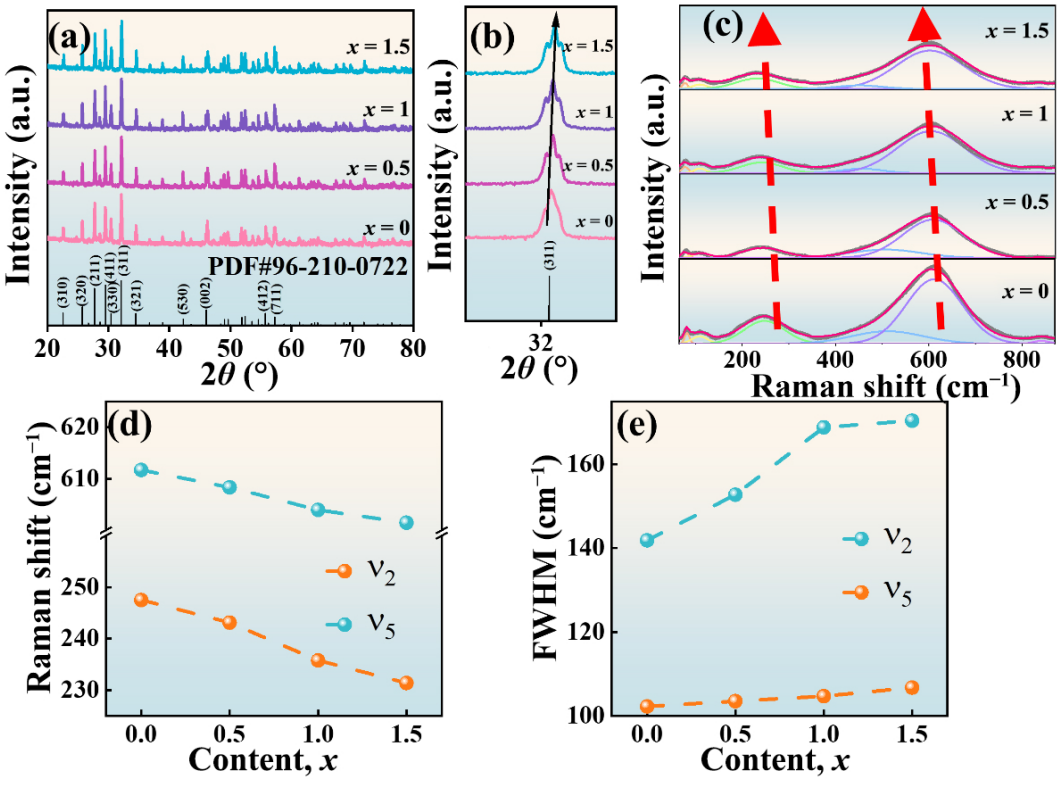

Fig. 2 (a) X-ray diffraction patterns of Ta_x ceramics, (b) enlarged view of $2\theta = 32°–33°$, and (c) Raman spectroscopy of Ta_x ceramics. (d) Variations in the wavenumbers of the ν_2 and ν_5 Raman vibrational modes. (e) FWHM in ν_2 and ν_5 modes.

Table 1 Crystallographic data of $Ba_{2.38}Sr_{2.12}Sm_{0.5}Gd_{0.5}Ti_1Zr_1Nb_{8-x}Ta_xO_{30}$ ceramics

	$x = 0$	$x = 0.5$	$x = 1$	$x = 1.5$
a (Å)	12.4857(0)	12.4835(1)	12.4831(4)	12.4707(1)
b (Å)	12.4857(0)	12.4835(1)	12.4831(4)	12.4707(1)
c (Å)	3.9291(8)	3.9222(4)	3.9221(2)	3.9222(8)
V (Å^3)	612.530(4)	611.234(1)	611.179(1)	609.987(5)

It is well established in the literature that the dielectric breakdown strength correlates with the grain size, as expressed by Eq. (2) [27,28]:

$$E_{BDS} \propto \frac{1}{\sqrt{G_a}} \tag{2}$$

where E_{BDS} is the dielectric breakdown strength, and G_a is the grain size. The microstructure of the ceramic samples was examined by scanning electron microscopy (SEM), as displayed in Figs. 3(a)–3(d). Figure 3(e) presents the corresponding grain size distributions that were statistically analyzed. All ceramic samples demonstrate homogeneous and compact microstructural features that are completely free from pore formation. With the gradual incorporation of Ta and the increase in configurational entropy, the average grain size in the ceramics decreased from 1.57 to 1.48 μm and then increased to 1.50 μm. The addition of Ta successfully restrains crystalline growth, yielding reduced average grain sizes [29]. Furthermore, the enhanced configurational entropy intensifies lattice distortion, which in turn hinders atomic migration and thereby promotes further grain refinement and an increased density of grain boundaries. Such microstructural refinement effectively homogenizes the distribution of applied electric fields within the ceramic materials. Collectively, these effects contribute to the superior dielectric breakdown performance observed [30].

Complex-impedance spectroscopy was employed to investigate the high E_b of Ta_x ceramics. In impedance spectroscopy, the polycrystalline ceramics are described by the brick-layer model, where the bulk material is represented as a network of conductive grains bounded by less conductive grain boundary regions [22]. The impedance data were fitted using an equivalent circuit model consisting of two series-connected parallel resistor–capacitor (R–C) elements, representing the grain and grain boundary responses, respectively. The equivalent circuit diagrams are shown in the insets in Figs. 4(a)–4(d), where R_b and C_b denote the grain resistance and capacitance, respectively, while R_{gb} and C_{gb} denote the grain boundary resistance and capacitance, respectively. The fitting procedure was performed with ZView software, and the measured data along with the optimized fitting results are presented in Figs. 4(a)–4(d). The measurements were conducted over a temperature range of 600–680 °C and a frequency range of 20 Hz to 1 MHz. The closely matched experimental and fitted impedance spectra confirm the validity of the equivalent circuit model. Figure 4(e) shows the impedance spectra of Ta_x ceramics at 600 °C, where a continuous enlargement of the arc radius is evident with increasing Ta content, pointing to a progressive increase in electrical resistance. This trend implies a synergistic effect of Ta doping and configurational entropy in strengthening the dielectric insulation, which subsequently leads to superior intrinsic breakdown strength and energy storage performance [31].

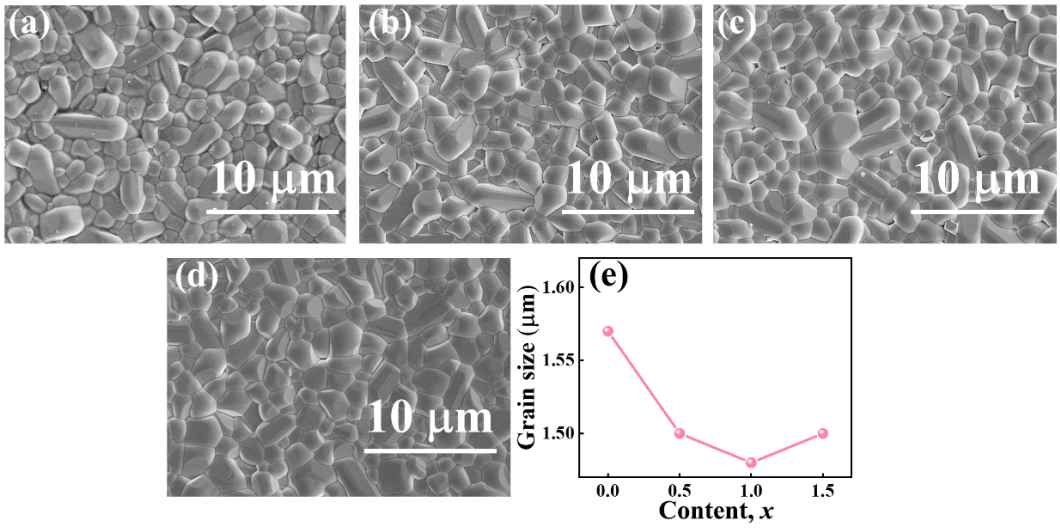

Fig. 3 (a–d) SEM images of Ta_x (x = 0, 0.5, 1, and 1.5) and (e) corresponding average grain size distributions.

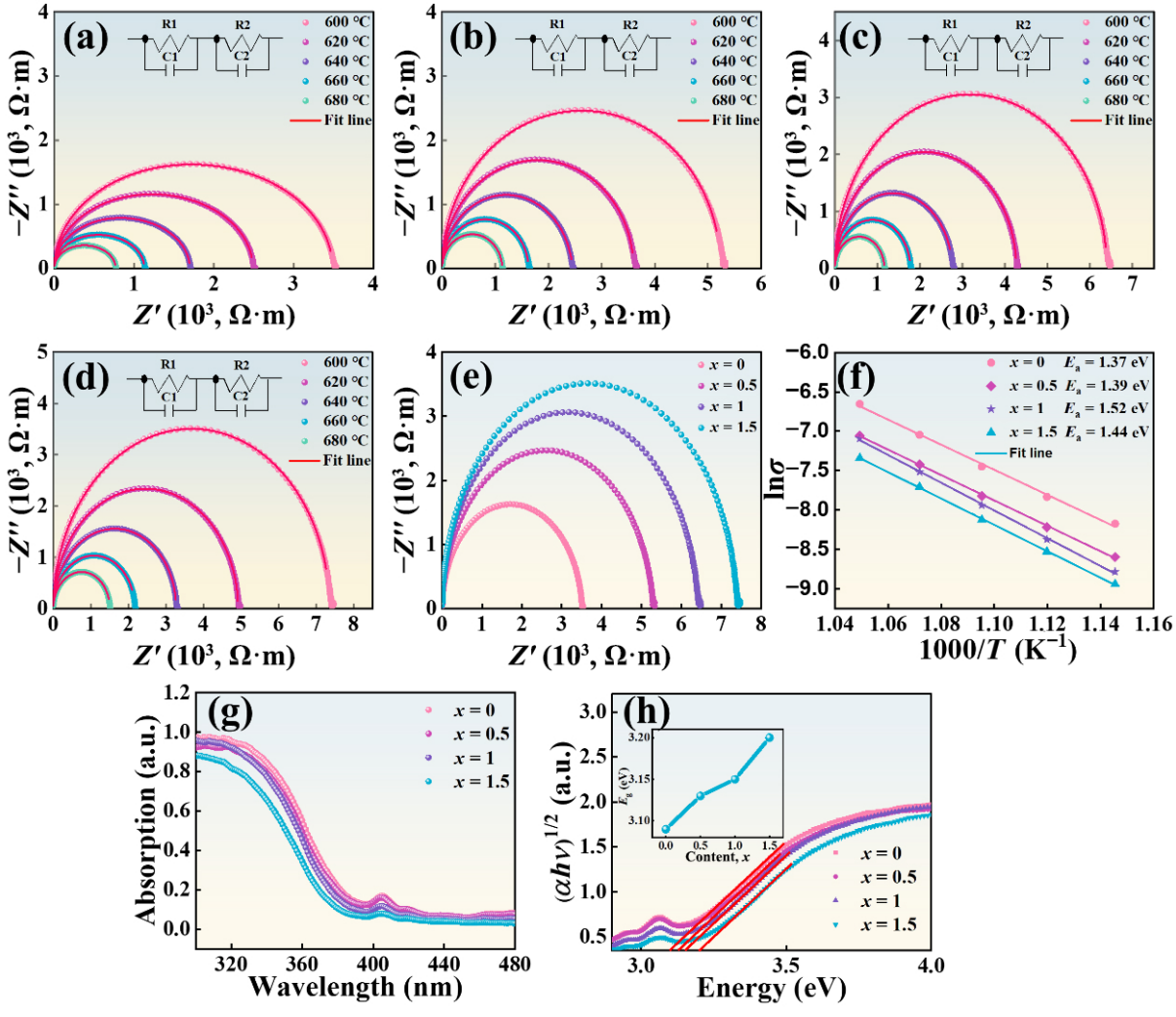

Fig. 4 (a–d) Complex Z^* plots of Ta_x (x = 0, 0.5, 1, and 1.5). (e) Complex Z^* plots for Ta_x at 600 °C. (f) Functional dependence of the natural logarithm of conductivity on the inverse temperature. (g) Absorption spectra from UV–Vis studies and (h) Tauc plots utilized for determining the bandgap energies.

The direct current activation energy (E_{dc}) linked to the direct current conduction in the dielectric ceramics can be determined from the Arrhenius relation (Eq. (3)) [32]:

$$\sigma = \sigma_0 \exp(-E_{dc}/(k_B T)) \quad (3)$$

The parameters in the Arrhenius law are defined as follows: σ denotes the bulk conductivity, σ_0 is the preexponential factor, T is the absolute temperature (K), and k_B is the Boltzmann constant (8.617×10^{-5} eV·K^{-1}). Figure 4(f) illustrates the dependence of lnσ on the reciprocal temperature, 1000/T. The direct current (DC)

conduction activation energy, E_{dc}, is equivalent to the slope derived from linear regression analysis. A nonmonotonic trend in E_{dc} values is observed under isothermal conditions with increasing Ta content, initially rising to peak values of 1.37, 1.39, 1.52, and 1.44 eV before decreasing. The reduction in oxygen vacancy concentration and the increase in grain boundary resistance lead to a rise in E_{dc}, which synergistically strengthens the intrinsic dielectric breakdown strength of the ceramic material. The judicious introduction of Ta reduces oxygen vacancies according to Eq. (4) [33]:

$$Ta_2O_5 + V_O'' \rightarrow 2Ta_{Ti^{4+}} + 5O_O^{\times} \quad (4)$$

The underlying mechanism can be summarized as follows: The suppressed oxygen vacancy concentration results in an increased E_{dc} for the $Ta_{0.5}$ ceramics. On the one hand, optimal Ta doping inhibits grain coarsening and increases grain boundary density, which enhances boundary resistivity and restricts oxygen vacancy hopping. On the other hand, it suppresses redox kinetics, thereby reducing the oxygen vacancy concentration. Nevertheless, a trade-off exists: The refractory nature of Ta means that excessive doping raises the sintering temperature, a common cause of oxygen vacancy formation in TTB-phase oxides that ultimately degrades the E_b [1,34].

The failure mechanism in dielectric materials is well documented to be primarily governed by electron-impact-induced breakdown, in which the bandgap serves as a key descriptor [35]. The optical bandgap can be determined using Eq. (5) [12]:

$$(ahv)^{(1/2)} = A(hv - E_g) \quad (5)$$

where a corresponds to the absorption coefficient, v symbolizes the frequency of incident light, h stands for Planck's constant, A is a material-related constant, and E_g indicates the bandgap energy of the semiconductor. The enlargement of E_g elevates the minimum energy required to excite electrons, consequently diminishing the likelihood of electron-driven breakdown [36]. In general, a broader bandgap makes it more difficult for electrons to jump from the valence band to the conduction band, thus rendering the material intrinsically more resistant to electrical conduction and endowing it with a higher dielectric breakdown strength. In insulating materials, the fundamental breakdown process is chiefly electronic in nature, and the bandgap width is a pivotal governing parameter in this mechanism [31,37]. As such, widening the bandgap is instrumental in boosting the energy storage characteristics of ceramic capacitors. The UV–Vis absorption spectra for the Ta_x ceramic series are provided in Fig. 4(g), and the direct bandgap values determined via Tauc plot analysis are summarized in Fig. 4(h). The progressive bandgap enlargement in Ta_x ceramics—from 3.09 (Ta_0) to 3.20 eV ($Ta_{1.5}$)—results from the higher intrinsic bandgap of Ta_2O_5 (~4.3 eV) compared to Nb_2O_5 (~3.4 eV) [38]. Dielectric failure is governed not only by electronic breakdown but also by avalanche processes. As avalanche breakdown arises from electron impact ionization, its breakdown strength strongly depends on the bandgap, as expressed by Eq. (6) [39]:

$$E = \frac{\Delta I}{q\lambda} \quad (6)$$

where ΔI represents the ionization energy (equivalent to bandgap width), q corresponds to the elementary charge, and λ designates the mean free path. Consequently, a larger bandgap hinders the generation of electron collisions and thus suppresses ionization, leading to a significant improvement in the dielectric breakdown strength.

Relaxor properties are essential for superior energy storage in ceramics. The relaxation dynamics of Ta_x ceramics were evaluated via frequency- (1 kHz–1 MHz) and temperature-dependent (−150 to 200 °C) measurements of permittivity and loss (Figs. 5(a)–5(d)). Elevated Ta content and configurational entropy consistently lower the permittivity while promoting relaxor behavior. The relaxor nature exhibits two key signatures: notable frequency dispersion, where the temperature of the permittivity maximum shifts upward with frequency, and significant dielectric broadening, implying a wide spectrum of relaxation times. For a more profound understanding of the underlying relaxation mechanisms, the dielectric dispersion data collected at 1 kHz were analyzed using a revised Curie–Weiss relationship, formulated as Eq. (7) [40]:

$$\ln\left(\frac{1}{\varepsilon} - \frac{1}{\varepsilon_m}\right) = \gamma \ln(T - T_m) \quad (7)$$

where ε is the relative permittivity, ε_m is the peak permittivity, T_m is the corresponding temperature, and γ is the diffuseness exponent (γ = 1–2), where larger values indicate stronger relaxor behavior [41]. The permittivity–temperature spectra measured at 1 kHz (Fig. 5(e)) shothat the $Ta_{0.5}$ composition attains the highest γ value of 1.55, confirming its pronounced relaxor properties. Accordingly, we applied the Vogel–Fulcher (V–F) relation to probe the dynamics of this relaxation process. The equation is given as Eq. (8) [12,42]:

$$f = f_0 \exp(-E_a/k_B(T_m - T_f)) \quad (8)$$

where E_a, f_0, and T_f signify the relaxation activation energy, Debye frequency, and freezing temperature, respectively. The fitting results are presented in Figs. 5(f)–5(i) and Table 2. At temperatures lower than T_f, dipole motion is arrested, forcing the system into a metastable condition. Consequently, surpassing T_f provides sufficient thermal energy to initiate dipole flipping. The calculated activation energies for these materials fall between 0.092 and 0.155 eV. A smaller E_a value indicates a lower potential barrier for polarization switching, which directly promotes a faster dipole response to alternating electric fields. From a micromechanism viewpoint, this barrier lowering arises from greater structural disorder at the local scale. This microscopic characteristic significantly enhances the capability for polarization reversal during ferroelectric cycling by reducing domain wall pinning, thus optimizing the material's recoverable energy density and release efficiency [12].

The development of cutting-edge applications utilizing dielectric substances demands exceptional overall energy storage properties as a fundamental requirement. For dielectric capacitors, the capability for energy storage is principally defined by the W_{rec} and energy storage efficiency (η). These parameters are determined through Eqs. (9)–(11) [43]:

$$W_{total} = \int_0^{P_{max}} E dP \quad (9)$$

$$W_{rec} = \int_{P_r}^{P_{max}} E dP \quad (10)$$

$$\eta = \frac{W_{rec}}{W_{total}} \times 100\% \quad (11)$$

where W_{total} denotes the overall recoverable energy density, P_{max} corresponds to the peak polarization, P_r indicates the remaining polarization, and E symbolizes the strength of the applied electric

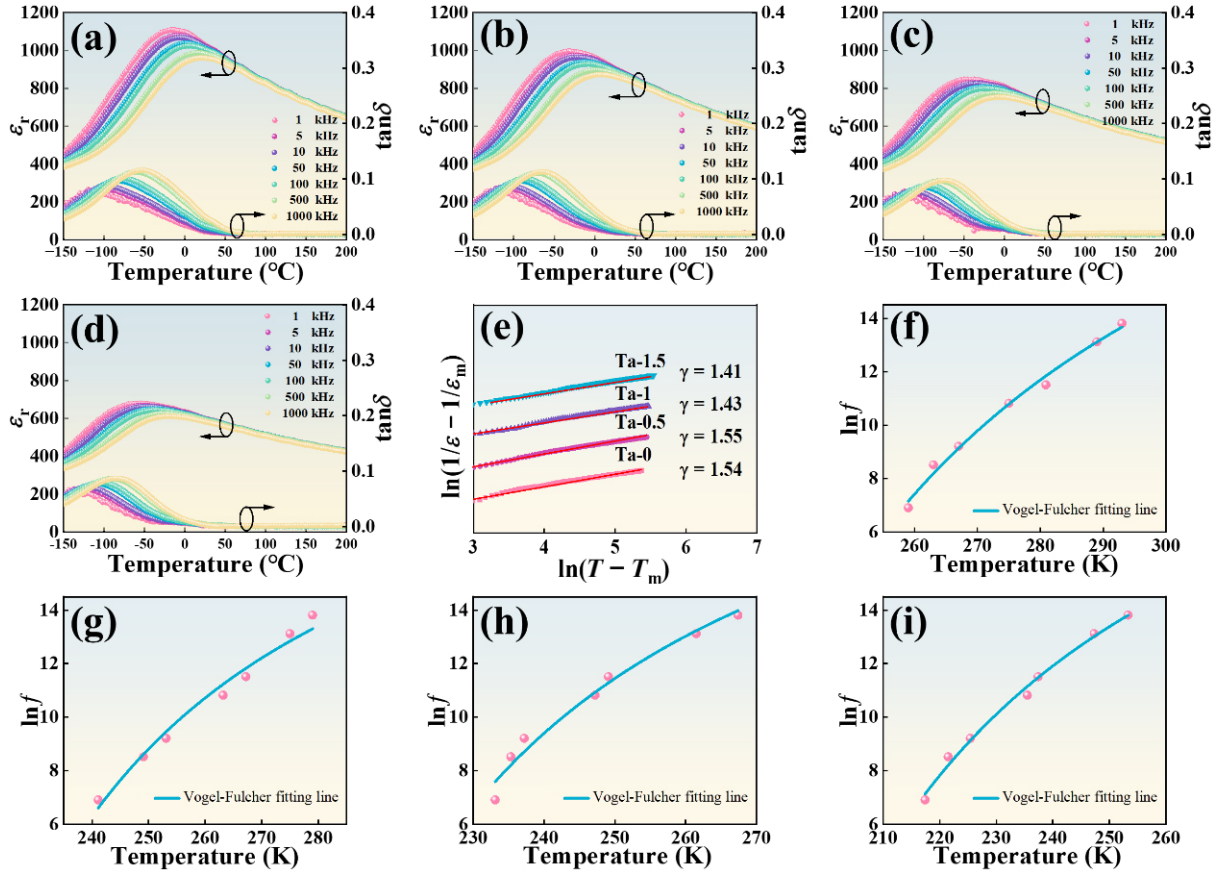

Fig. 5 (a–d) Dielectric constant and loss of Ta_x ceramics (x = 0, 0.5, 1, and 1.5) as a function of temperature. (e) Fitting results using the Curie–Weiss law corrected with a 1 kHz dielectric constant. (f–i) Vogel-Fulcher fitting results of Ta_x (x = 0, 0.5, 1, and 1.5).

Table 2 Data obtained from fitting the permittivity at 1 kHz

	x = 0	x = 0.5	x = 1	x = 1.5
E_a (eV)	0.155	0.097	0.092	0.129
T_f (K)	177.73	177.99	172.56	143.84

field. Consequently, attaining outstanding energy storage characteristics is critically dependent on a set of pivotal elements: an elevated P_{max}, a minimized P_r, and a substantial E_b [44]. To probe the energy storage properties of Ta_x (x = 0, 0.5, 1, and 1.5) ceramic specimens, Figs. 6(a) and 6(b) display the energy storage performance of the ceramic samples. The synergistic effect of Ta-induced grain refinement, bandgap widening, and increased resistivity collectively enhances the E_b of the ceramics. Finally, the breakdown strength of the $Ta_{0.5}$ ceramics was measured to be 830 kV·cm^{-1}, a recoverable energy density of 7.93 J·cm^{-3}, and η maintained a high level of 94.25%. To investigate the temperature-dependent energy storage properties of the $Ta_{0.5}$ ceramics, polarization–electric (P–E) hysteresis loops were measured under an electric field of 500 kV·cm^{-1} over a temperature range of 30 to 180 °C. The results are presented in Fig. 6(c), and the related energy storage parameters at various temperatures are shown in Fig. 6(d). The results indicate that the $Ta_{0.5}$ ceramics exhibit excellent thermal stability, with an efficiency of 93% at room temperature, which then decreases to 87.5% at 180 °C. A comparison of the energy storage properties between the present work and other TTB ceramics is presented in Fig. 6(e) [1,12,14,21,31,45–66]. This comparative analysis makes it apparent that the incorporation of a high-entropy approach within this TTB system to enhance energy storage performance is a viable methodology.

Relative to other energy storage capacitors, ceramic-based devices demonstrate exceptionally rapid discharge durations ($t_{0.9}$) together with substantial power density (P_D). To assess the charge–discharge characteristics of these components, experiments were carried out on ceramic specimens, with emphasis placed on the released energy density (W_{dis}), current density (C_D), and associated power density. The parameters W_{dis}, C_D, and P_D are obtainable through Eqs. (12)–(14) [12,14]:

$$W_{dis} = \frac{R_L \int i^2(t)\mathrm{d}t}{V} \tag{12}$$

$$C_D = \frac{I_{max}}{S} \tag{13}$$

$$P_D = \frac{EI_{max}}{2S} \tag{14}$$

where R_L indicates the load resistance, V signifies the specimen volume, I_{max} is the maximum discharge current during the charge/discharge process, E is the applied electric field strength, and S refers to the functional electrode region covered by silver paste. Findings from overdamped evaluations are displayed in Figs. 7(a)–7(d). With increasing Ta concentration and configurational entropy, the W_{dis} of ceramic materials subjected to a 440 kV·cm^{-1} electric field shows an initial enhancement from 4.10 to 5.20 J·cm^{-3}, subsequently declining to 4.56 and 4.37 J·cm^{-3}. In parallel, the insets in Figs. 7(a)–7(d) depict that the discharge duration ($t_{0.9}$) initially extends from 1.16 to 1.56 μs and then contracts to 1.21 and 1.34 μs. The considerable W_{dis} and ultrafast $t_{0.9}$ observed in $Ta_{0.5}$ ceramics indicate their suitability for use in

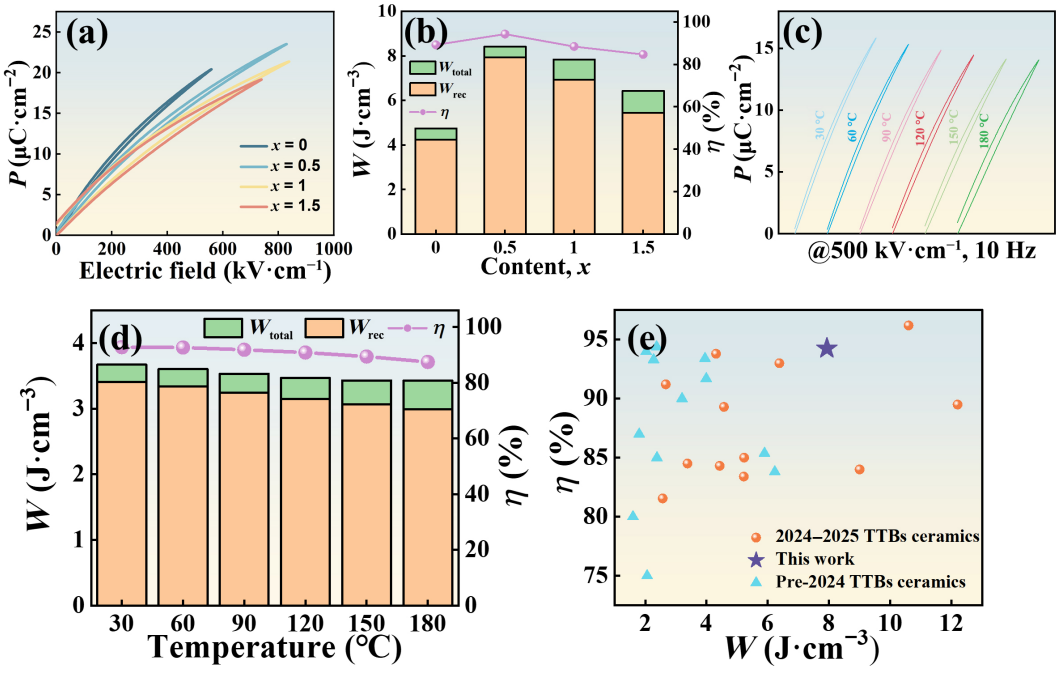

Fig. 6 (a) *P*–*E* hysteresis loops, (b) recoverable energy density and efficiency, (c) temperature-dependent *P*–*E* hysteresis loops of the $Ta_{0.5}$ ceramics, and (d) variation in recoverable energy density and efficiency with temperature. (e) Performance comparison between this work and reported TTB ceramics.

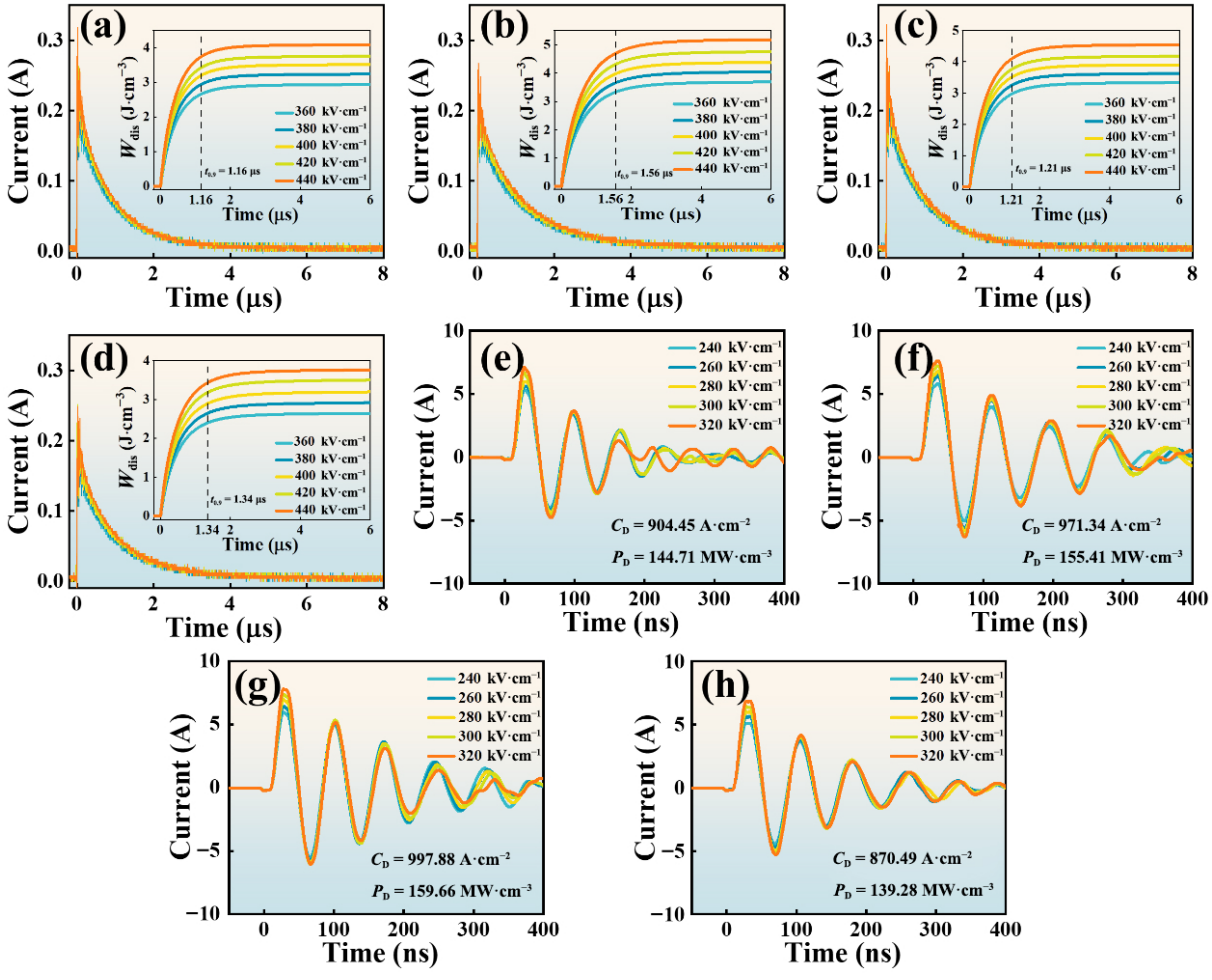

Fig. 7 (a–d) Overdamped state and $t_{0.9}$ (inset) of Ta_x ceramics (x = 0, 0.5, 1, and 1.5). (e–h) Underdamped state of Ta_x ceramics (x = 0, 0.5, 1, and 1.5).

rapid charge–discharge pulsed power capacitors. Underdamped pulsed discharge profiles for Ta_x ceramics across electric fields of 240–320 kV·cm^{-1} are provided in Figs. 7(e)–7(h). The maximum discharge current displays a growing tendency with a

strengthening electric field. For the $Ta_{0.5}$ ceramics, a peak current of 7.63 A was reached, from which a current density of 971.34 A·cm^{-2} and a power density of 155.41 MW·cm^{-3} were calculated. Additionally, investigations were performed on the thermal stability of the charge/discharge characteristics for ceramic specimens. The W_{dis} values recorded at 300 kV·cm^{-1} under different temperature conditions are provided in Figs. S5(a)–S7(d) in the ESM. Throughout the temperature range of 30 to 180 °C, the variation rate of W_{dis} for $Ta_{0.5}$ remained at approximately 10%, indicating remarkable thermal stability. These findings demonstrate that Ta_x ceramics are promising candidates for pulse power systems.

The microstructure of samples Ta_0 and $Ta_{0.5}$ was investigated using TEM, and the relevant results are shown in Figs. 8(a)–8(f). Figures 8(a) and 8(d) present the SAED patterns obtained along the [110] zone axis for ceramics Ta_0 and $Ta_{0.5}$, respectively, which exhibit characteristic fundamental diffraction spots typical of a TTB-type substructure. In addition to the Bragg reflections corresponding to the TTB structure, superlattice spots related to structural modulation (indicated by orange arrows) appear in the SAED patterns, suggesting the presence of incommensurate modulation in ceramics Ta_0 and $Ta_{0.5}$ at room temperature. Studies have shown that the existence of commensurate modulation structures is closely associated with long-range order and demonstrates ferroelectric characteristics, whereas the presence of incommensurate modulation implies pronounced relaxor behavior. The incommensurate modulation wave vector can be expressed as $(1/4 + \delta)(\boldsymbol{a} - \boldsymbol{b}) + 1/2\boldsymbol{c}$, where $\boldsymbol{a}$, $\boldsymbol{b}$, and $\boldsymbol{c}$ represent reciprocal lattice vectors, and δ is a parameter describing the deviation from commensurate periodicity. δ is determined by the formula $\delta = (x - y)/(x + y)$, where x and y denote the distances between adjacent incommensurate diffraction spots, and their values are obtained from measurements of weak diffraction peak positions. The inset in Fig. 8(a) illustrates the method for measuring the incommensurability parameter (δ). Based on calculations from weak diffraction peaks, it was found that δ_{Ta0} = 0.21 (300 K) and $\delta_{Ta0.5}$ = 0.27 (300 K). The increase in the incommensurability parameter originates from A-site disorder, which further leads to the broadening of satellite diffraction spots. Doping with Nb^{5+} inevitably induces oxygen octahedral distortion,

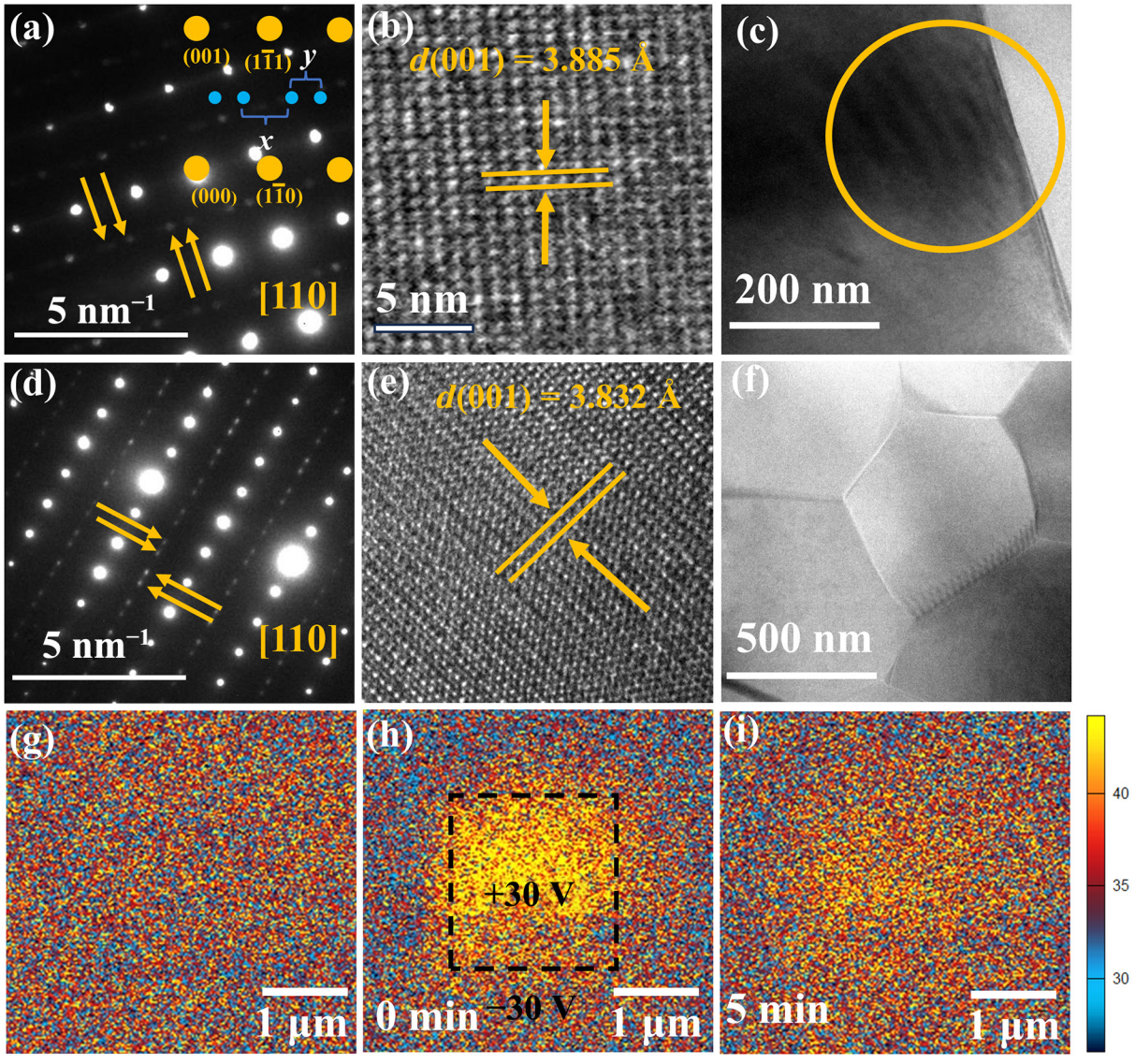

Fig. 8 TEM characterization of Ta_0 and $Ta_{0.5}$ ceramics. (a–c) Ta_0 ceramics show (a) SAED pattern ([110] zone axis), (b) HRTEM image, and (c) domain structure. (d–f) $Ta_{0.5}$ ceramics show (d) SAED pattern ([110] zone axis), (e) HRTEM image, and (f) domain structure. (g) PFM amplitude image of the $Ta_{0.5}$ ceramics over a 4 μm × 4 μm area. Corresponding phase images after domain poling under different conditions: (h) 30 V and 0 min; (i) 30 V and 5 min.

清華大学出版社 Tsinghua University Press | SciOpen

resulting in local lattice strain. This suggests that B-site ion doping tends to promote incommensurate modulation. The HRTEM images in Figs. 8(b) and 8(e) reveal the lattice fringe spacings corresponding to the (110) planes in the Ta_0 and $Ta_{0.5}$ ceramics. As the unit cell contracts from Ta_0 to $Ta_{0.5}$, the interplanar spacing decreases from 3.885 to 3.832 Å. These values closely align with the interplanar spacings of the corresponding planes in the standard TTB-type SBN structure (PDF#96-210-0722, *P4bm*). As shown in Figs. 8(c) and 8(f), the Ta_0 sample exhibits obvious long-range continuous polarization, manifested as ferroelectric domains with widths reaching several tens of nanometers. In contrast, the $Ta_{0.5}$ sample exhibits a notable difference, lacking well-defined ferroelectric domain structures. This absence may be attributed to the smaller size of the nanodomains in this sample, which renders them difficult to resolve using conventional TEM, as reported in the literature [13,67]. This observation is further illustrated in Fig. 8(f).

PFM serves as a powerful technique for probing electric-field-induced domain configurations and their corresponding behaviors. The domain pattern on the surface of $Ta_{0.5}$ ceramics is displayed in Fig. 8(g) [68]. Only weak PFM signals were detected, primarily due to the diminishment of domain dimensions to the nanoscale, which falls below the instrument's resolution capability. To further explore the transient domain evolution and relaxation processes in Ta-0.5, localized poling tests were conducted via PFM lithography mode (area: 4 μm × 4 μm, voltage: ±30 V), with outcomes illustrated in Fig. 8(h). When subjected to ±30 V, both the density of switched domains and the strength of the domain reaction remained comparatively low. This phenomenon arises from the substantial energy barrier (high relaxation activation energy, E_a) linked to the weakly correlated dipole interactions within $Ta_{0.5}$, combined with their pronounced reversibility. Figure 8(i) depicts the out-of-plane PFM phase profile for $Ta_{0.5}$. Strengthened random-field effects generate an intrinsic recovery force in the material, enabling switched PNRs to rapidly return to their original condition after approximately 5 min. As a result, $Ta_{0.5}$ ceramics achieve minimal P_r, which is advantageous for macroscopic energy storage applications [69].

4 Conclusions

In this study, ceramics with the composition $Ba_{2.38}Sr_{2.12}Sm_{0.5}Gd_{0.5}Ti_1Zr_1Nb_{8-x}Ta_xO_{30}$ (x = 0, 0.5, 1, and 1.5) were synthesized using the solid-state reaction method. By integrating high-entropy design principles with bandgap engineering, the synergistic combination of high-entropy design and bandgap engineering led to a substantial enhancement in the performance of the SBN. First, the disruption of long-range ferroelectric order effectively suppressed grain growth and increased the resistivity of the ceramics. This was realized through precise compositional and structural tailoring, which substantially widened the bandgap. The enhanced bandgap, in turn, led to a remarkable enhancement of the breakdown field strength. Notably, the $Ba_{2.38}Sr_{2.12}Sm_{0.5}Gd_{0.5}Ti_1Zr_1Nb_{7.5}Ta_{0.5}O_{30}$ ceramics exhibited outstanding energy storage performance. It achieved a recoverable energy density of 7.93 J·cm^{-3} at 830 kV·cm^{-1} with an efficiency of 94.25%. Under overdamped conditions at 440 kV·cm^{-1}, this ceramic delivered a discharge energy density of 5.20 J·cm^{-3} with an ultrafast discharge time ($t_{0.9}$) of 1.56 μs. Under underdamped conditions at 320 kV·cm^{-1}, a high current density (C_D = 971.34 A·cm^{-2}) and power density (P_D = 155.41 MW·cm^{-3}) were achieved. Moreover, the ceramics exhibited excellent thermal stability, with the discharge energy varying by less than 10% (ΔW_{dis} < 10%) across a temperature range of 30–180 °C. These results demonstrate the application potential of this ceramic in pulse power devices.

Acknowledgements

The authors thank the National Natural Science Foundation of China (No. 12164012) and the Science and Technology Plan of Guangxi (Nos. AA25069001 and AD25069100) for financial support.

Availability of data and materials

The data that support the findings of this study are available from the corresponding author upon reasonable request.

Competing interests

The authors have no competing interests to declare that are relevant to the content of this article.

Electronic Supplementary Material

Supplementary material is available in the online version of this article at https://doi.org/10.26599/JAC.2026.9221260.

References

[1] Cao L, Yuan Y, Li EZ, *et al.* Relaxor regulation and improvement of energy storage properties of $Sr_2NaNb_5O_{15}$-based tungsten bronze ceramics through B-site substitution. *Chem Eng J* 2021, **421**: 127846.

[2] Jin Z, Zheng X, Zhu Z, *et al.* Enhanced triboelectric degradation of organics by tuning the synergy between ferroelectric polarization and illumination. *Mater Today* 2023, **29**: 101427.

[3] Jain A, Wang YG, Guo H. Microstructure induced ultra-high energy storage density coupled with rapid discharge properties in lead-free $Ba_{0.9}Ca_{0.1}Ti_{0.9}Zr_{0.1}O_3$–$SrNb_2O_6$ ceramics. *Ceram Int* 2021, **47**: 487–499.

[4] Jin ZH, Lu ML, Jiang C, *et al.* Mechanocatalytic H_2O_2 production using ferroelectric $KSr_2Nb_3Ta_2O_{15}$ nanorods. *Nano Energy* 2025, **138**: 110892.

[5] He B, Zhou B, Yan SG, *et al.* Ultrahigh energy density and efficiency $BaTiO_3$-based multilayer ceramic capacitors. *J Adv Ceram* 2025, **14**: 9221018.

[6] Long CB, Su ZQ, Xu AW, *et al.* High energy storage performance in the $Bi_{0.5}Na_{0.5}TiO_3$–$BaTiO_3$–$Nd(Mg_{1/2}Hf_{1/2})O_3$ ternary system with multiscale polymorphic domains and local heterogeneous structure. *J Adv Ceram* 2025, **14**: 9221063.

[7] Wu SY, Fu B, Zhang JJ, *et al.* Superb energy storage capability for $NaNbO_3$-based ceramics featuring labyrinthine submicro-domains with clustered lattice distortions. *Small* 2023, **19**: 2303915.

[8] Wang H, Wu SY, Fu B, *et al.* Hierarchically polar structures induced superb energy storage properties for relaxor $Bi_{0.5}Na_{0.5}TiO_3$-based ceramics. *Chem Eng J* 2023, **471**: 144446.

[9] Jayakrishnan AR, Silva JPB, Kamakshi K, *et al.* Are lead-free relaxor ferroelectric materials the most promising candidates for energy storage capacitors. *Prog Mater Sci* 2023, **132**: 101046.

[10] Dai SW, Li MY, Wu XW, *et al.* Combinatorial optimization of perovskite-based ferroelectric ceramics for energy storage applications. *J Adv Ceram* 2024, **13**: 877–910.

[11] Hu ZD, Liu Z, Han B, *et al.* Designing silver niobate-based relaxor antiferroelectrics for ultrahigh energy storage performance. *J Adv Ceram* 2024, **13**: 1282–1290.

[12] Tang LP, Ning WZ, Wu S, *et al.* Energy storage performance of high-entropy SBN-based tungsten bronze-structure ceramic. *J Alloys Compd* 2025, **1015**: 178902.

[13] Chen L, Long FX, Qi H, *et al.* Outstanding energy storage performance in high-hardness $(Bi_{0.5}K_{0.5})TiO_3$-based lead free relaxors via multi-scale synergistic design. *Adv Funct Mater* 2022, **32**: 2110478.

[14] Dan YJ, Tang LP, Ning WZ, *et al.* Achieving enhanced energy

storage performance and ultra-fast discharge time in tungsten–bronze ceramic. *J Adv Ceram* 2024, **13**: 1349–1358.
[15] Qian J, Liu Y, He LQ, *et al.* Topological bubble domain engineering for high strain response. *Sci Adv* 2025, **11**: 8840.
[16] Qian J, Ge GL, Cai ZM, *et al.* Constructing topological vortex domains in polar nano-regions enables high-capacitive energy storage. *Adv Mater* 2026, **38**: 18813.
[17] Liu HB, Dkhil B. Origin of the crossover from ferroelectric to relaxor in tetragonal tungsten bronzes. *J Alloys Compd* 2022, **929**: 167314.
[18] Li C, Zhang YP, Liu J, *et al.* Long-range and local structure of $Sr_xBa_{1-x}Nb_2O_6$ (x = 0.33 and 0.67) across the ferroelectric–relaxor transition. *Chem Mater* 2020, **32**: 1844–1853.
[19] Xiang HM, Xing Y, Dai FZ, *et al.* High-entropy ceramics: Present status, challenges, and a look forward. *J Adv Ceram* 2021, **10**: 385–441.
[20] Qi H, Chen L, Deng SQ, *et al.* High-entropy ferroelectric materials. *Nat Rev Mater* 2023, **8**: 355–356.
[21] Duan JH, Wei K, Du QB, *et al.* High-entropy tungsten bronze ceramics for large capacitive energy storage with near-zero losses. *Adv Funct Mater* 2024, **34**: 2409446.
[22] Gao YF, Song ZZ, Hu HC, *et al.* Optimizing high-temperature energy storage in tungsten bronze-structured ceramics via high-entropy strategy and bandgap engineering. *Nat Commun* 2024, **15**: 5869.
[23] Chen L, Yu HF, Wu J, *et al.* Large energy capacitive high-entropy lead-free ferroelectrics. *Nano-Micro Lett* 2023, **15**: 65.
[24] Wang Y, Sun TL, Zhu XL, *et al.* Ferroelectric transition and structural modulation in $Sr_2Na(Nb_{1-x}Tax)_5O_{15}$ tungsten bronze ceramics. *J Appl Phys* 2021, **129**: 244107.
[25] Zhu XL, Chen XM. Ferroelectric transition of $Sr_5SmTi_3Nb_7O_{30}$ tungsten bronze ceramics investigated using differential scanning calorimetry and Raman scattering. *J Am Ceram Soc* 2012, **95**: 3185–3191.
[26] Qi H, Xie AW, Tian A, *et al.* Superior energy-storage capacitors with simultaneously giant energy density and efficiency using nanodomain engineered $BiFeO_3$–$BaTiO_3$–$NaNbO_3$ lead-free bulk ferroelectrics. *Adv Energy Mater* 2020, **10**: 1903338.
[27] Tunkasiri T, Rujijanagul G. Dielectric strength of fine grained barium titanate ceramics. *J Mater Sci Lett* 1996, **15**: 1767–1769.
[28] Gao YF, Zhu XP, Yang B, *et al.* Grain size modulated $(Na_{0.5}Bi_{0.5})_{0.65}Sr_{0.35}TiO_3$-based ceramics with enhanced energy storage properties. *Chem Eng J* 2022, **433**: 133584.
[29] Albino M, Heijboer P, Porcher F, *et al.* Metastable ferroelectric phase and crossover in the $Ba_2NdFeNb_{4-x}Ta_xO_{15}$TTB solid solution. *J Mater Chem C* 2018, **6**: 1521–1534.
[30] Chen ZB. Designs where disorder prevails. *Science* 2024, **384**: 158–159.
[31] Yang B, Gao YF, Lou XJ, *et al.* Remarkable energy storage performances of tungsten bronze $Sr_{0.53}Ba_{0.47}Nb_2O_6$-based lead-free relaxor ferroelectric for high-temperature capacitors application. *Energy Storage Mater* 2023, **55**: 763–772.
[32] Rawat M, Yadav KL. Compositional effects on structural, dielectric, ferroelectric and transport properties of $Ba_{1-x}(Bi_{0.5}Li_{0.5})_xTiO_3$ ceramics. *Mater Chem Phys* 2014, **148**: 655–663.
[33] Xu D, Zhou XY, Yu TL, *et al.* The phase composition, dielectric, and energy storage performance of A-site vacancy modulated $BaTiO_3$ ceramics with $Bi(In_{1/2}(Li_{0.5}Ta_{0.5})_{1/2})O_3$ modification. *Ceram Int* 2024, **50**: 50469–50483.
[34] Bian JJ, Otonicar M, Spreitzer M, *et al.* Structural evolution, dielectric and energy storage properties of $Na(Nb_{1-x}Ta_x)O_3$ ceramics prepared by spark plasma sintering. *J Eur Ceram Soc* 2019, **39**: 2339–2347.
[35] Guo J, Yu HF, Ren YF, *et al.* Multi-symmetry high-entropy relaxor ferroelectric with giant capacitive energy storage. *Nano Energy* 2023, **112**: 108458.
[36] Shi JP, Chen XL, Li X, *et al.* Realizing ultrahigh recoverable energy density and superior charge–discharge performance in $NaNbO_3$-based lead-free ceramics via a local random field strategy. *J Mater Chem C* 2020, **8**: 3784–3794.
[37] Cao L, Yuan Y, Zhang X, *et al.* Relaxor nature and energy storage properties of $Sr_{2-x}M_xNaNb_{5-x}Ti_xO_{15}$ (M = La^{3+} and Ho^{3+}) tungsten bronze ceramics. *ACS Sustain Chem Eng* 2020, **8**: 17527–17539.
[38] Kondo JN, Iguchi A, Tanaka M, *et al.* Surface properties of Ta_2O_5 layers prepared on SBA-15. *Catal Today* 2012, **192**: 197–202.
[39] Zhao L. A formula to calculate solid dielectric breakdown strength based on a model of electron impact ionization and multiplication. *AIP Adv* 2020, **10**: 025003.
[40] Jiang XW, Hao H, Zhou JJ, *et al.* Optimized energy storage properties of $BaTiO_3$-based ceramics with enhanced grain boundary effect. *J Mater Sci-Mater El* 2021, **32**: 14328–14336.
[41] Balmuchu SP, Dobbidi P. Temperature-dependent broadband dielectric and ferroelectric properties of $Ba_{(1-x)}Sr_xTiO_3$ ceramics for energy storage capacitor applications. *J Mater Sci-Mater El* 2021, **32**: 9623–9639.
[42] Ye JM, Wang GS, Zhou MX, *et al.* Excellent comprehensive energy storage properties of novel lead-free $NaNbO_3$-based ceramics for dielectric capacitor applications. *J Mater Chem C* 2019, **7**: 5639–5645.
[43] Feng WB, Zhu XL, Liu XQ, *et al.* Relaxor nature in $Ba_5RZr_3Nb_7O_{30}$ (R = La, Nd, Sm) tetragonal tungsten bronze new system. *J Am Ceram Soc* 2018, **101**: 1623–1631.
[44] Feng WB, Cheng LL, Hua XN, *et al.* Dielectric property and energy storage performance enhancement for iron niobium based tungsten bronze ceramic. *RSC Adv* 2022, **12**: 33816–33824.
[45] Xu SD, Han MZ, Zhu ZP, *et al.* Excellent energy-storage performance realized in SANNS-based tungsten bronze ceramics *via* synergistic optimization strategy. *J Materiomics* 2025, **11**: 100930.
[46] Riaz MF, Hussain F, Chandio AD, *et al.* Remarkable energy storage performance in lead-free tungsten bronze ferroelectrics for high temperature applications. *Chem Eng J* 2025, **522**: 167263.
[47] Ma KL, Cui JY, Li JS, *et al.* Multiple collaborative optimization strategy regulates tungsten bronze ceramics to achieve efficient energy storage performance. *J Energy Storage* 2025, **134**: 118203.
[48] Qiao WJ, Lou XJ, Gao YF, *et al.* High-performance energy storage in tungsten bronze-based ferroelectric ceramics under low electric field. *J Eur Ceram Soc* 2026, **46**: 117786.
[49] Zhang XZ, Wang HL, Bu XY, *et al.* Simultaneously realizing superior energy storage properties and outstanding charge-discharge performances in tungsten bronze-based ceramic for capacitor applications. *Inorg Chem* 2021, **60**: 6559–6568.
[50] Xu SD, shen SJ, Hao R, *et al.* Relaxor nature and superior energy storage performance of $Sr_2Ag_{0.2}Na_{0.8}Nb_5O_{15}$-based tungsten bronze ceramics through B-site substitution. *Chem Eng J* 2022, **433**: 133812.
[51] Zheng X, Jin ZH, Dan YJ, *et al.* Relaxation behavior and energy storage of A-site substituted $Sr_{4-x}Na_{2-x}La_xTa_{0.6}Nb_{9.4}O_{30}$ ferroelectric ceramics. *J Mater Sci-Mater El* 2023, **34**: 148.
[52] Cao L, Yuan Y, Meng XJ, *et al.* Ferroelectric-relaxor crossover and energy storage properties in $Sr_2NaNb_5O_{15}$-based tungsten bronze ceramics. *ACS Appl Mater Inter* 2022, **14**: 9318–9329.
[53] Xu SD, Shen SJ, Huang CW, *et al.* Enhancing energy storage performance in lead-free bismuth sodium niobate-based tungsten bronze ceramics through relaxor tuning. *ACS Appl Mater Inter* 2023, **15**: 11642–11651.
[54] Li SW, Wang Y, Guo L, *et al.* Enhanced energy storage performance in SBNN-based tungsten bronze ceramics through co-substitution strategy in A/B sites. *J Alloys Compd* 2023, **963**: 171044.
[55] Li SW, Yan Z, You YF, *et al.* Enhancement of energy storage and luminescent performances in tungsten bronze multifunctional ceramics. *Ceram Int* 2024, **50**: 14223–14231.
[56] Wan RF, Zhang HF, Sheng LS, *et al.* Outstanding energy density and charge–discharge performances in $Sr_2KNb_5O_{15}$-based tungsten bronze ceramics for dielectric capacitor applications. *Ceram Int* 2024, **50**: 37126–37135.

[57] Hou ST, Wang X, Liu X, *et al.* Significant increase in comprehensive energy storage performances of $Ca_{0.5}(Sr_{0.5}Ba_{0.5})_2Nb_5O_{15}$-based tungsten bronze relaxor ceramics. *J Eur Ceram Soc* 2023, **43**: 6854–6863.
[58] Luo C, Zhu CH, Liang YH, *et al.* Promoting energy storage performance of $Sr_{0.7}Ba_{0.3}Nb_2O_6$ tetragonal tungsten bronze ceramic by a two-step sintering technique. *ACS Appl Electron Mater* 2022, **4**: 452–460.
[59] Luo C, Zheng XT, Zheng P, *et al.* Realizing excellent energy storage performances in tetragonal tungsten bronze ceramics via a B-site engineering strategy. *J Alloys Compd* 2023, **933**: 167809.
[60] Liu JM, Jiang Y, Zhang WC, *et al.* Ferroelectric tungsten bronze-based ceramics with high-energy storage performance via weakly coupled relaxor design and grain boundary optimization. *Nat Commun* 2024, **15**: 8651.
[61] Peng HN, Liu Z, Fu ZQ, *et al.* Superior energy density achieved in unfilled tungsten bronze ferroelectrics via multiscale regulation strategy. *Adv Sci* 2023, **10**: 2300227.
[62] Dan YJ, Zheng X, Meng YZ, *et al.* Simultaneously achieving large energy storage density and high efficiency in the optimized $Sr_2NaNb_5O_{15}$ system with excellent temperature stability at a low electric field. *Ceram Int* 2024, **50**: 6801–6813.
[63] Feng W, Zhu X, Chen X. Crystal structure, dielectric, and ferroelectric characteristics of zirconate tantalate ceramics with tungsten bronze structure. *J Mater Sci Mater El* 2021, **32**: 7481–90.
[64] Peng HN, Wu TT, Liu Z, *et al.* High-entropy relaxor ferroelectric ceramics for ultrahigh energy storage. *Nat Commun* 2024, **15**: 5232.
[65] Yang B, Gao YF, Li JR, *et al.* Tailoring Zr-doped tungsten bronze (Sr, Ba,Gd)Nb_2O_6 relaxor ferroelectric with high electrical insulation interface for dielectric capacitor. *Compos Part B-Eng* 2024, **271**: 111189.
[66] Gao YF, Qiao WJ, Lou XJ, *et al.* Ultrahigh energy storage in tungsten bronze dielectric ceramics through a weakly coupled relaxor design. *Adv Mater* 2024, **36**: 2310559.
[67] Xie JM, Ning WZ, Tang LP, *et al.* A multiple collaborative optimization strategy for enhanced energy storage and ultrafast discharge performance in tungsten bronze ceramics. *Ceram Int* 2026, **52**: 7359–7371.
[68] Dong XY, Wu XJ, Lv X, *et al.* Enhancing energy storage performances of $Bi_{0.5}Na_{0.5}TiO_3$-based dielectric ceramics via modulating polymorphic polar nanoregions. *J Mater Chem A* 2024, **12**: 21772–21781.
[69] Pan Y, Zhang Y, Dong QP, *et al.* High-entropy engineered $Bi_{0.47}Na_{0.47}Ba_{0.06}TiO_3$-based weakly coupled relaxor ferroelectrics with quasi-linear polarization for enhanced energy storage performance. *Chem Eng J* 2025, **512**: 162551.